Acta Cryst. (1978). A**34**, 684–698

The Crystal Structure of η-Cu_3Si Precipitates in Silicon

BY JAN KETIL SOLBERG*

Department of Physics, University of Oslo, Blindern, Oslo, Norway

(*Received* 11 *May* 1977; *accepted* 13 *March* 1978)

The crystal structure of Cu–Si precipitates in silicon has been studied by means of transmission electron diffraction and microscopy. The precipitates are shown to be of the equilibrium Cu_3Si phase, probably of the low-temperature η'' form. Consistent with earlier X-ray diffraction data for this phase, the crystal structure of the precipitates is determined to be based on a trigonally distorted b.c.c. arrangement. The lattice is orthorhombic (C), and is a two-dimensional long-period superlattice, which it is suggested is based on the intermediate-temperature η' phase; lattice parameters $a_{\eta''} = 76{\cdot}76$, $b_{\eta''} = 7{\cdot}00$, $c_{\eta''} = 21{\cdot}94$ Å. On the basis of the diffraction data for the precipitates, it is suggested that the η and η' phases are both trigonal, space groups $R\bar{3}m$ and $R\bar{3}$ respectively, with lattice parameters $a_\eta = 2{\cdot}47$ Å, $\alpha_\eta = 109{\cdot}74°$ and $a_{\eta'} = 4{\cdot}72$ Å, $\alpha_{\eta'} = 95{\cdot}72°$.

1. Introduction

When copper-doped dislocation-free silicon is cooled from high temperature, star-shaped agglomerates of small precipitate particles form. Each arm of the star consists of a planar distribution of particles, enveloped by an edge dislocation. These precipitate colonies have been the subject of numerous investigations, and their morphology as well as their growth mechanism can be considered well established (Rieger, 1964; Fiermans & Vennik, 1965, 1967*a*,*b*; Nes & Washburn, 1971, 1972, 1973; Nes & Solberg, 1973*a*,*b*; Solberg & Nes, 1978*a*,*b*).

However, on the crystal structure of the precipitate particles no detailed analysis has been presented. A complete structure analysis is difficult to perform because the precipitates occupy only 10^{-4}–10^{-5} of the total scattering volume. X-ray diffraction reveals, therefore, no scattering from the precipitates. Electron microscope studies by Nes & Washburn (1971) and Das (1973) conveyed some information, but owing to the very limited experimental data none of the crystal structures (cubic) proposed by these authors can be accepted without a further experimental confirmation.

In the work of Nes & Washburn and Das a lot of information in the diffraction patterns has been lost as a result of the heavy background scattering from relatively thick foils. By studying precipitate colonies located close to the edges of very thin foils (some few 1000 Å) the present author has obtained additional electron diffraction data indicating a complicated superstructure. By comparing these results with earlier data on Cu_3Si, the precipitates have been identified with the η''-Cu_3Si phase, which is the equilibrium phase at room temperature. The crystal structures of the three Cu_3Si polymorphs are unknown, but by assuming that η'' is a long-period superstructure based on the other two, the diffraction data from the precipitates has been utilized for suggesting structures for η and η' as well. The experimental results and the analysis leading to the crystal structures for the three Cu_3Si polymorphs are given in this report. Although not justified until § 4.1, the precipitate spot indices are labelled η'' throughout the article.

* Present address: Central Institute for Industrial Research, Blindern, Oslo, Norway.

2. Experimental

A Czochralski-grown dislocation-free silicon single crystal was used in the investigation. ⟨211⟩-surface foils containing copper precipitates were prepared by methods described elsewhere (Nes & Washburn, 1971; Solberg & Nes, 1978*a*). The specimens were examined in a Philips EM 300 electron microscope operating at 100 kV.

The reciprocal lattice of the precipitates was examined by tilting the specimen systematically about a low-index axis. Because only the very strongest precipitate reflections could be seen on the fluorescent screen in the microscope, a diffraction pattern was recorded after each 1° of tilt. To distinguish between diffraction spots from different precipitates within the selection aperture, a series of dark-field images from individual spots were recorded. To decide whether a spot was a real spot or due to multiple scattering, the foil was tilted around the respective reciprocal vector. Because of the low intensity in diffraction this tilting was performed while the dark-field contrast from the reflection was studied. The same tilting technique was frequently employed in order to prevent strong spots outside the objective aperture from contributing to the

contrast in dark-field images (through diffuse scattering, Gjønnes & Solberg, 1978).

3. Results

3.1. *Diffraction data*

Figs. 1 and 2 show the two most densely populated reciprocal-lattice planes for the precipitate structure, coinciding with the matrix projections $(121)^*_{Si}$ and $(011)^*_{Si}$. Only the strongest reflections are visible on the photographic copies, so the details in the patterns are made clear in the drawings (*b*), in which all the reflections observed with small variations in the diffraction conditions are plotted. In both figures, rows of closely spaced precipitate reflections are seen parallel to the $[1\bar{1}1]^*_{Si}$ direction. The distance between the reflections along a row is $\frac{1}{7}|[1\bar{1}1]^*_{Si}|$ (within the experimental error).

On the left of Fig. 1(*b*) the reflections along each row are numbered consecutively. The distance from the origin to each row of reflections can, within the experimental error, be given in multiples of $\frac{1}{20}|[\bar{2}02]^*_{Si}|$, which is done at the top of Fig. 1(*b*). This serves as a numbering of the rows. The relative intensities of the rows are given at the top, and the approximate intensity distribution *along* the rows is indicated on the right. The rows 0, 5, 14 and 19 are by far the strongest rows.

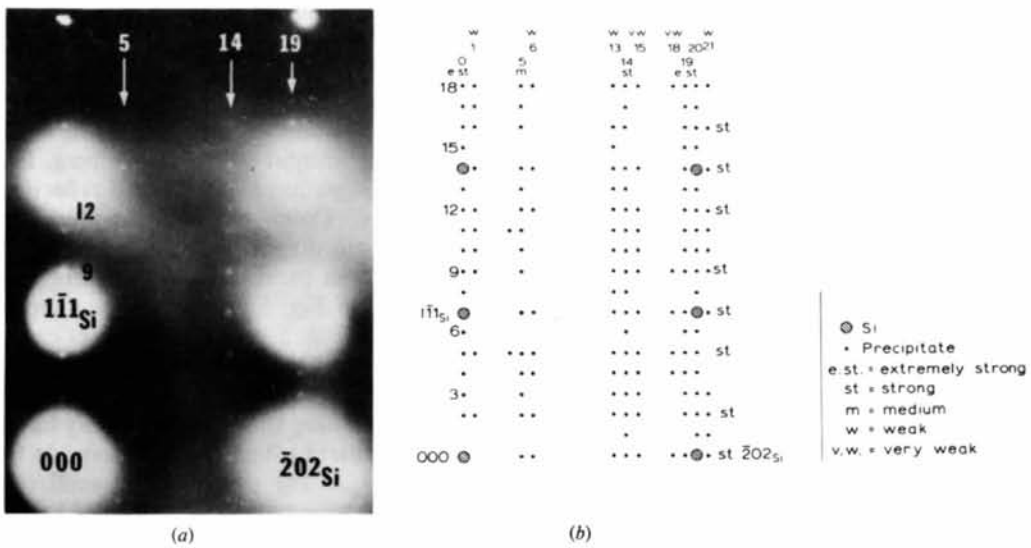

(*a*) (*b*)

Fig. 1. (*a*) Precipitate reflections in the $(121)^*_{Si}$ projection. In (*b*) all the observed precipitate reflections in the projection are plotted.

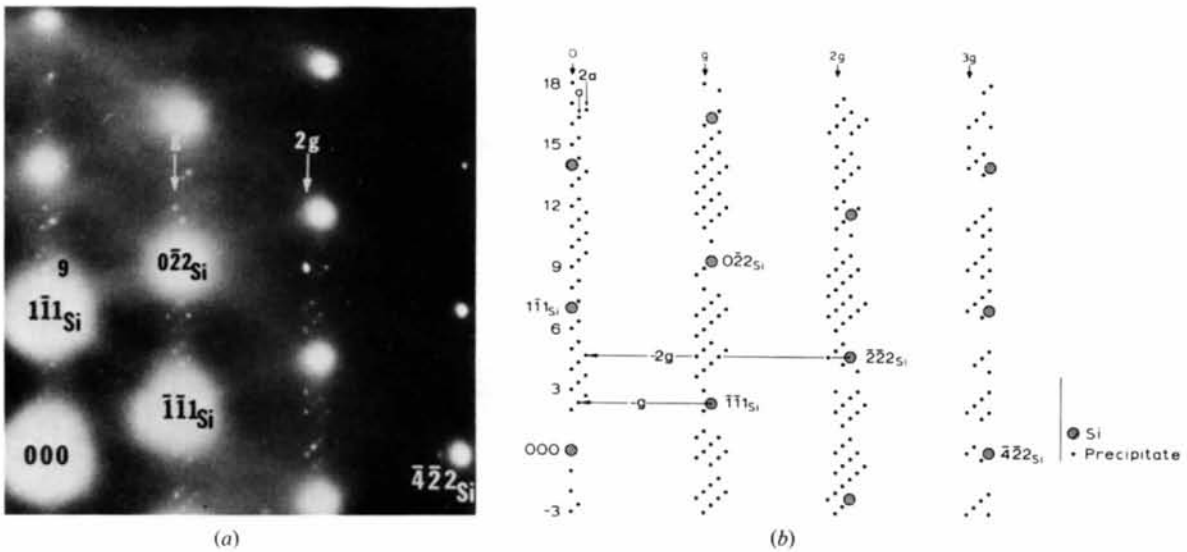

(*a*) (*b*)

Fig. 2. (*a*) Precipitate reflections in the $(011)^*_{Si}$ projection. In (*b*) all the observed precipitate reflections in the projection are plotted.

The high intensity of row 20 in Fig. 1(*a*) is due to double diffraction.

The other rows which are plotted in Fig. 1(*b*) were visible only when the projection was near or completely in a symmetrical orientation. Multiple scattering processes may therefore have contributed to the observed intensities of these rows.

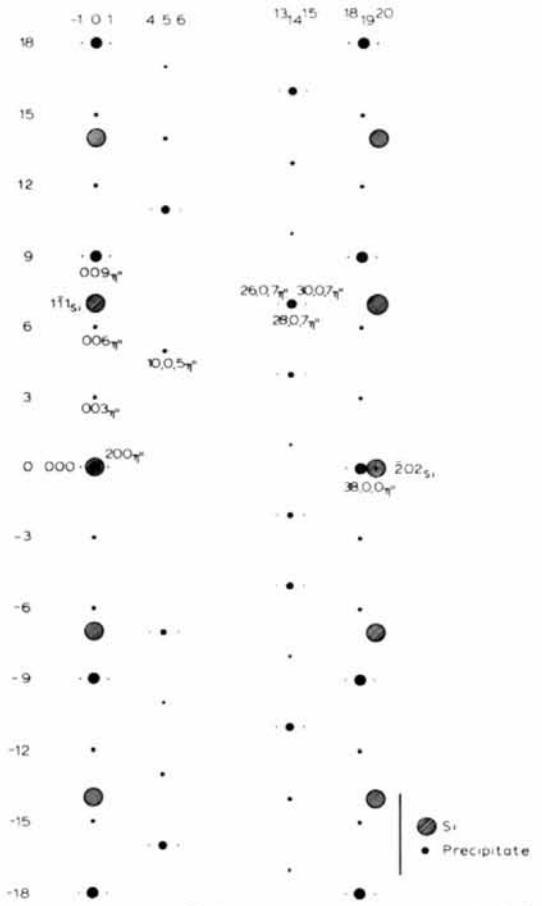

Fig. 3. Single-crystal $(0\bar{1}0)^*_{\eta''}$ diffraction pattern in the $(121)^*_{Si}$ projection. Observed intensities along the very weak rows are probably mainly due to multiple scattering.

A detailed experimental examination resolved the precipitate diffraction patterns of Figs. 1 and 2 into contributions from two equivalently oriented orthorhombic base-centered lattices, plus multiply diffracted spots. One of the single-crystal patterns contained in Fig. 1 is indexed in Fig. 3. The reflections are drawn on a scale corresponding to the observed intensities. Note the fading intensities close to the origin along row 5. The single-crystal pattern was extracted on the basis of a dark-field analysis of the reflections along the strong rows 5, 14 and 19. Fig. 4 gives an example from row 14. Fig. 4(*a*) and (*b*) are dark-field images from the reflections -5 and 5, and illustrate the two equivalent orientations of the precipitate lattice (precipitates *A* and *B*). The intensity distribution along row $00l_{\eta''}$ was obtained from a precipitate with a slight misorientation with respect to the matrix, so that no double diffraction from the matrix contributed to the reflections. (For further experimental details, see Solberg, 1975.)

In Fig. 3 we have also plotted reflections from the weak rows. Owing to the possibility of multiple scattering into these rows, few experimental facts were obtained about them. However, micrographs like that reproduced in Fig. 5 provided strong support for their existence. In Fig. 5 very sharp fringes can be observed on precipitate *A* in a dark-field image recorded with the spots $10,0,11_{\eta''}$ and $8,0,11_{\eta''}$ within the objective aperture. So sharp fringes could hardly have occurred if multiple scattering had been responsible for the weak spot $8,0,11_{\eta''}$. The only multiple-scattering sequence which could have generated spot $8,0,11_{\eta''}$ is

$$8,0,11_{\eta''} = 20\bar{2}_{Si} + 38,0,0_{\eta''} + 10,0,11_{\eta''}.$$

The projection was almost in a symmetrical orientation during the exposure; so, owing to the relatively large

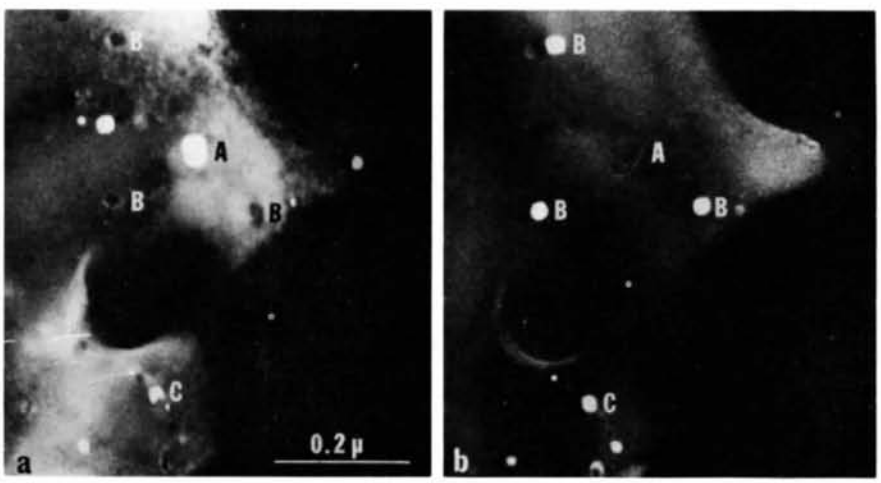

Fig. 4. Dark-field micrographs from the reflections (*a*) -5 and (*b*) 5 along row 14 in the $(121)^*_{Si}$ projection. (Note that precipitate *C* is bright in both micrographs, § 3.3.)

excitation error of the $20\bar{2}_{Si}$ spot, the fringes on the precipitates are unlikely to have been caused by this scattering process.

In Fig. 2, only the rows g, $2g$ and $3g$ contain allowed precipitate reflections. These reflections are common to the orientations A and B, and in Fig. 6 they are indexed in accordance with the pattern of Fig. 3. All the other reflections vanished when the foil was tilted out from the symmetrical orientation given by Fig. 2(a). Of these rows, rows a and $2a$ in Fig. 2(b) can be explained as a result of double scattering of $-g$ and $-2g$ from the parallel rows of matrix reflections through $\bar{1}\bar{1}1_{Si}$ and $2\bar{2}2_{Si}$ respectively. Similar scattering processes can account for the other rows.

The orthorhombic reciprocal lattice which can be deduced from Figs. 3 and 6 is shown viewed along $[00\bar{1}]_{\eta''} = \frac{1}{3}[\bar{1}1\bar{1}]_{Si}$ in Fig. 7. The different symbols denote rows of reflections normal to the paper, and from each row, the reflection closest to the plane $(001)^*_{\eta''}/(1\bar{1}1)^*_{Si}$ (containing the origin) is indexed. Precipitate spot rows which are equivalent to the rows 19 and 5/14 are indicated by filled circles and large crosses respectively. The dots and small crosses symbolize the weak rows equivalent to those in Fig. 3.

In real space the lengths of the unit axes are $a_{\eta''} = 76{\cdot}76$, $b_{\eta''} = 7{\cdot}00$, $c_{\eta''} = 21{\cdot}94$ Å, and the orientation relationship to the matrix is:

$$(100)_{\eta''} \| (\bar{1}01)_{Si}; (001)_{\eta''} \| (1\bar{1}1)_{Si}.$$

3.2. *The intensity distribution in reciprocal space*

The intensity distribution in reciprocal space is summarized in Table 1 and Fig. 7. Table 1 lists the intensities along the strongest rows in the $(0\bar{1}0)^*_{\eta''}$ plane. To simplify the table the intensity value (zero) for the invisible spots between those plotted in Fig. 3 is omitted. The weak rows in the projection are supposed to exhibit the same intensity distribution as the nearest strong row. Because of multiple scattering there exist no certain experimental data for these rows.

In Fig. 7 are given the relative intensities of the strong rows in reciprocal space, as observed during a

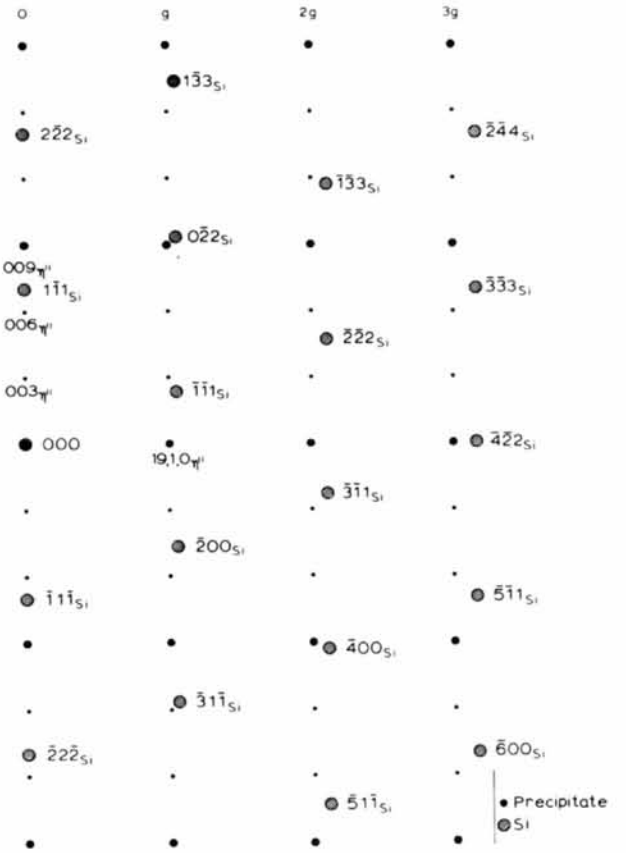

Fig. 6. Precipitate $(1,\bar{1}9,0)^*_{\eta''}$ diffraction pattern in the $(011)^*_{Si}$ projection. Along each row parallel to $[001]^*_{\eta''}$, every third reflection is strong and those in between are weak.

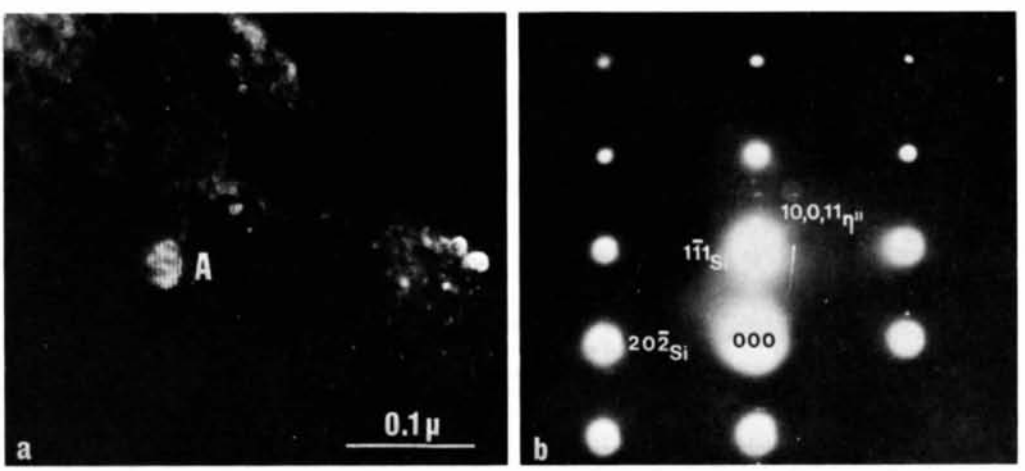

Fig. 5. Interference contrast from the reflections $10,0,11_{\eta''}$ and $8,0,11_{\eta''}$. Only the strongest spot $10,0,11_{\eta''}$ is visible within the objective aperture.

systematic tilting experiment. The intensity distribution along the individual rows is identical for rows given by the same l value. The distributions along rows identified by opposite l values are identical, but reversed relative to each other, as the l values indicate. Exceptions from this general pattern are rows $10,0,l_{\eta''}$ and $91l_{\eta''}$ which both exhibit fading intensities close to the origin (*cf.* Fig. 3).

3.3. *Polycrystalline precipitates*

The precipitate lattice can be oriented in several equivalent ways with respect to the matrix, and all the rows deduced from Fig. 7 by 60 and 120° rotations about $[001]^*_{\eta''}$ were observed. A dark-field analysis revealed that the rows belonging to the two rotated orientations consist of reflections from the same precipitates as the rows of Fig. 7. This is interpreted as being caused by polycrystalline precipitates. The reciprocal pattern consisting of all the precipitate A reflections is so complicated that it is very unlikely to originate from a single crystal. That would have involved a three-dimensional long-period superstructure, and so far such structures have not been discovered.

Supporting experimental evidence for polycrystalline precipitates is given in Figs. 4 and 8, the former showing dark-field images from the reflections −5 and 5 along row 14 in the $(121)^*_{Si}$ projection. Since precipitate C is bright in both micrographs, it must contain crystals with different orientations, corresponding to those of A and B. Fig. 8 shows an example of moiré fringes which abruptly change direction within the precipitate. The operating reflections are $\bar{2}20_{Si}$ and a strong precipitate spot on the inside of this. The micrographs in Fig. 8 (*a*) and (*b*) were recorded with small differences in the diffraction conditions. It is reasonable to attribute the abrupt change in fringe direction to different crystals within the precipitate. The fringe shift is less probably caused by a bending of the atom planes across the particle/matrix interface due to the mismatch between the two lattices. No matrix strain contrast has been observed around the precipitates, indicating that interface dislocations compensate for the differences in the lattice constants. Moreover, a

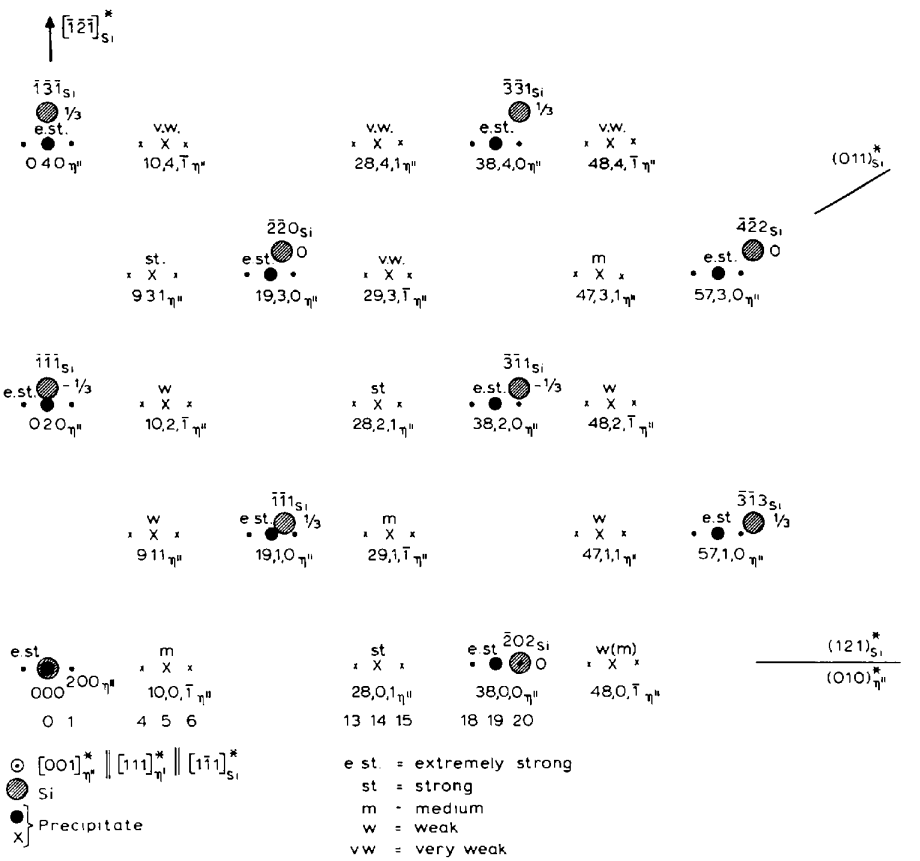

Fig. 7. The reciprocal lattice of the precipitates indexed according to a base-centered (C) orthorhombic lattice. The reciprocal lattice is projected normal to the plane $(001)^*_{\eta''} \| (111)^*_{Si}$. Along each 'high-intensity' row of precipitate reflections the observable reflection closest to $(001)^*_{\eta''}$ (containing the origin) is indexed. The observed relative intensities of these rows are given (see § 3.2). The indexed matrix reflections are those lying closest to the $(1\bar{1}1)^*_{Si}$ plane; their distances from the plane are given as fractions of $|[1\bar{1}1]^*_{Si}|$.

continuous bending of crystal planes should not result in such abrupt shifts in the fringe direction as observed in this case. A similar observation to that in Fig. 8, indicative of three crystals within one single precipitate, has also been made.

3.4. *The atomic composition of the precipitates*

No currently available experimental technique has a resolution capable of determining the composition of the precipitates. Even the probe obtained in the electron microscope using a scanning attachment does probably not give a satisfactory space resolution for exact measurements. However, based on the knowledge of the precipitate growth mechanism an estimate of the composition can be made. The growth occurs by repeated nucleation on an edge dislocation, which emits vacancies during climb. The area of the extra half plane gives the number of vacancies absorbed by the precipitates during growth. By measuring this area, F, and the total volume of the precipitates, V, the composition of the precipitates can be estimated from the expression (Solberg, 1975):

$$\text{Atomic \% Si} = \frac{100 \cdot 8v(V - Fb)}{a^3 V}\ \%,$$

where v is the atomic volume of the precipitate phase, a is the silicon lattice parameter, and b is the length of the Burgers vector of the enveloping dislocation [$\mathbf{b} = a\langle 110\rangle/2$ (Nes & Washburn, 1971)]. The atomic volume v is unknown, but by choosing the value 12 Å^3, which is roughly the value for the known intermediate Cu–Si phases, the Si content in the precipitates was found to be about 25 at.%. The absolute experimental uncertainty involved in this estimate (mainly attached to the measurement of V) is 5–10 at.%. A value of 25 at.% Si corresponds to the composition of Cu_3Si. (For a detailed discussion of this estimate, see Solberg, 1975, pp. 87–89.)

Table 1. *Observed relative intensities, I_{obs}, of η'' reflections in the $(0\bar{1}0)^*_{\eta''}$ projection*

hkl	I_{obs}*	*hkl*	I_{obs}*	*hkl*	I_{obs}*	*hkl*	I_{obs}*
0,0,18	*e.st.*	10,0,18		28,0,18		38,0,18	*e.st.*
17		17	*v.w.*	17		17	
16		16		16	*st*	16	
15	*w*	15		15		15	*w*
14		14	*w*	14		14	
13		13		13	*w*	13	
12	*w*	12		12		12	*w*
11		11	*st(m)*	11		11	
10		10		10	*v.w.*	10	
9	*e.st.*	9		9		9	*e.st.*
8		8	0	8		8	
7		7		7	*v.st.*	7	
6	*w*	6		6		6	*w*
5		5	*w(m)*	5		5	
4		4		4	*m*	4	
3	*w*	3		3		3	*w*
2		2	~0	2		2	
1		1		1	*v.w.*	1	
000	dir. beam	10,0,0		28,0,0		38,0,0	*e.st.*
$\bar{1}$		$\bar{1}$	~0	$\bar{1}$		$\bar{1}$	
$\bar{2}$		$\bar{2}$		$\bar{2}$	*m*	$\bar{2}$	
$\bar{3}$	*w*	$\bar{3}$		$\bar{3}$		$\bar{3}$	*w*
$\bar{4}$		$\bar{4}$	~0	$\bar{4}$		$\bar{4}$	
$\bar{5}$		$\bar{5}$		$\bar{5}$	*st*	$\bar{5}$	
$\bar{6}$	*w*	$\bar{6}$		$\bar{6}$		$\bar{6}$	*w*
$\bar{7}$		$\bar{7}$	*m*	$\bar{7}$		$\bar{7}$	
$\bar{8}$		$\bar{8}$		$\bar{8}$	*v.w.*	$\bar{8}$	
$\bar{9}$	*e.st.*	$\bar{9}$		$\bar{9}$		$\bar{9}$	*e.st.*
$\bar{10}$		$\bar{10}$	*v.w.*	$\bar{10}$		$\bar{10}$	
$\bar{11}$		$\bar{11}$		$\bar{11}$	*st*	$\bar{11}$	
$\bar{12}$	*w*	$\bar{12}$		$\bar{12}$		$\bar{12}$	*w*
$\bar{13}$		$\bar{13}$	*w*	$\bar{13}$		$\bar{13}$	
$\bar{14}$		$\bar{14}$		$\bar{14}$	*w*	$\bar{14}$	
$\bar{15}$	*w*	$\bar{15}$		$\bar{15}$		$\bar{15}$	*w*
$\bar{16}$		$\bar{16}$	*st*	$\bar{16}$		$\bar{16}$	
$\bar{17}$		$\bar{17}$		$\bar{17}$	*v.w.*	$\bar{17}$	
0,0,18	*e.st.*	10,0,18		28,0,18		38,0,18	*e.st.*

* *e.st.* = extremely strong, *v.st.* = very strong, *st* = strong, *m* = medium, *w* = weak, *v.w.* = very weak. When no value is specified, the observed intensity is zero.

4. Discussion

4.1. *A comparison with the diffraction data for* Cu_3Si

Cu_3Si should be the equilibrium phase precipitated from a silicon matrix supersaturated with copper. The crystal structure of this phase is not known, but the available experimental data show great resemblance to the diffraction data on the precipitate structure obtained in the present work.

An X-ray powder analysis of the low-temperature Cu_3Si phase has been performed by Arrhenius & Westgren (1931), using iron $K\alpha_{1,2}$ and $K\beta$ radiation. They found that the strongest lines in the powder diagram plus some of the other lines satisfied the hexagonal equation

$$\sin^2\theta = 0{\cdot}0758(h^2 + hk + k^2) + 0{\cdot}157l^2;$$

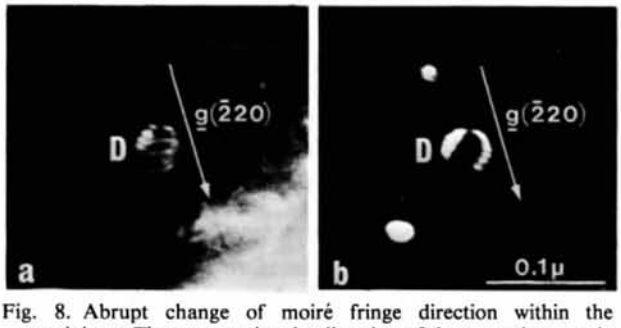

Fig. 8. Abrupt change of moiré fringe direction within the precipitate. The arrows give the direction of the operating matrix reflection. A strong precipitate spot is located on the inside of this reflection.

θ is the Bragg angle for the *hkl* reflection. A series of weak lines did not, however, satisfy the equation. From these results and from the intensity distribution it was concluded that the phase has a hexagonal lattice and a structure which deviates only slightly from a body-centered cubic structure, like those of γ-brass and α-manganese. A later investigation by Schubert & Braundauer (1952) confirmed these results, and it was suggested that Cu_3Si has a trigonally deformed b.c.c. structure and is isotypic with the high-temperature phase of Cu_3Ge (distorted $A2$). Neither of these works gives any lattice parameters, but the following hexagonal parameters can be calculated from the equation given above: $a_h = 4{\cdot}05$, $c_h = 2{\cdot}44$ Å. More detailed information on the crystal structure of Cu_3Si does not exist.

For the precipitate structure, the 'extremely strong' reflections along the rows $00l_{\eta''}$, $38,0,l_{\eta''}$ and $19,1,l_{\eta''}$ define a hexagonal reciprocal sublattice. The parameters for the corresponding lattice in real space are $a = 4{\cdot}04$, $c = 2{\cdot}44$ Å. These values are practically equal to the above values for a_h and c_h. Hence, the precipitates seem to be identical to the equilibrium Cu_3Si phase. Further evidence for this conclusion is the existence of weak powder-diagram lines which did not fit in with the hexagonal lattice, as reported by Arrhenius & Westgren. Neither do most of the reflections from the precipitates. Moreover, in the previous section the Si concentration in the precipitates was estimated to be about 25 at.%, which is in excellent agreement with the composition of the Cu_3Si phase. From these facts we conclude that the two phases are identical.

The diffraction pattern in Fig. 3 resembles in many respects those characteristic for long-period superstructures. The split spots in the $[\bar{1}01]^*_{Si}$ direction are striking, and the intensity distribution parallel to $[1\bar{1}1]^*_{Si}$ is very similar to that obtained from long-period superlattices in close-packed metals (Sato, Toth & Honjo, 1967). We have therefore concluded that the precipitate structure, as it exists at room temperature, arises from periodic displacements in two perpendicular directions in an ordered superstructure. Such a solution agrees well with the equilibrium diagram (Mima & Hasegawa, 1960; Elliot, 1965). The Cu–Si compounds are regarded as electron phases (Massalski & King, 1961; Hume-Rothery & Raynor, 1954), and the η-Cu_3Si phase has been reported to have three polymorphs (Mima & Hasegawa, 1960). Long-period superlattices are common in electron phase systems, and they are usually the low-temperature form of polymorphic phases (Sato & Toth, 1961). The room-temperature form of the precipitates is therefore assumed to belong to the low-temperature η'' phase, even though they probably grew as high-temperature η particles in the temperature range 800–630°C (Nes & Washburn, 1973). The probability of a phase transformation from the high-temperature phase during cooling is also emphasized by other authors (Mima & Hasegawa, 1960; Schubert & Brandauer, 1952).

In further analogy with common electron compounds, we ascribe a disordered structure to the high-temperature η phase, and an ordered superstructure to the intermediate-temperature phase η'. To consider η as a solid solution is in accordance with assumptions made by Mima & Hasegawa (1956, 1957, 1960).

None of the three polymorphs has a known crystal structure. The only experimental data previously available on Cu_3Si are those presented in § 4.1. Those data refer most probably to the same phase as that investigated in this work, but have been connected with the η' structure (Schubert & Brandauer, 1952; Hansen, 1958). That connection was, however, made without considering the transformation $\eta' \leftrightarrow \eta''$, and as mentioned by Mima & Hasegawa (1960), the data may refer to the η'' structure, as assumed in this work.

The room-temperature form of the precipitates is suggested to arise from periodic displacements in the η' superstructure, through the transformations $\eta \rightarrow \eta' \rightarrow \eta''$ during cooling. It is very difficult to solve the long-period superstructure without a knowledge of the two other structures. Therefore, from the intensity peaks in the η'' reciprocal space, we first sought a reciprocal lattice for η and η'. The crystal structures for the three polymorphs we arrived at in this way are discussed in the sections below.

4.2. *The fundamental η structure*

There are substantial reasons for associating the rhombohedral distribution of 'extremely strong' precipitate spots right on the inside of matrix reflections ($\bar{2}02_{Si}$, $0\bar{2}2_{Si}$, $\bar{4}00_{Si}$, $\bar{4}\bar{2}2_{Si}$; Figs. 3 and 6) with the fundamental lattice. Because of their location it was hard to obtain the true intensity of all these spots, and a distinction between the spots graded 'extremely strong' has previously not been made. There are, however, several observations indicating that the spots on the inside of matrix reflections are *extraordinarily* strong, *e.g.* the spot $38,4,9_{\eta''}$ in Fig. 9(*a*) which is indexed according to the mentioned rhombohedral lattice in Fig. 9(*b*). It is seen to be much stronger than the 'extremely strong' spot $38,4,0_{\eta''}$ which fulfils the Bragg condition in Fig. 9(*a*). It is also worth noticing that all the spots discovered by Nes & Washburn (1971) and Das (1973) were strong ones inside matrix reflections.

The precipitate spot in the direction of $\bar{5}\bar{1}\bar{1}_{Si}$ in Fig. 9(*c*) arrives from precipitate *A*, as 201_η in Fig. 9(*b*) does. It has about the same intensity as 201_η, but does not belong to the rhombohedral lattice mentioned above. However, the reflection can be indexed according to a fundamental lattice with a twin relationship to that giving reflections inside Si spots. This interpretation is in accordance with previous observations

of twins in the η phase (Mima & Hasegawa, 1957, 1960), and is also in line with the conclusions made on polycrystalline precipitates in § 3.3. The observation of Fig. 9(*c*) is thus in favour of the suggested fundamental reciprocal lattice. Observations analogous to that in Fig. 9(*a*)–(*c*) have been made in other projections as well, including $(011)^*_{Si}$. Note for instance the extremely strong twin fundamental spot along row 2*g*, level with $0\bar{2}2_{Si}$ in Fig. 2(*a*). It can be indexed $1\bar{1}1_{\eta twin}$; *cf.* next section where the twin formation is discussed in more detail.

Following the above discussion, we attach a rhombohedral structure to the disordered η phase. The space group is $R\bar{3}m$, and the lattice parameters are $a_\eta = 2{\cdot}47$ Å, $\alpha_\eta = 109{\cdot}74°$, provided that no expansion or contraction of the lattice follows the ordering or periodic displacements. There is one atom per unit cell, and the atomic positions correspond to the atomic and octahedral sites in the two f.c.c. lattices constituting the Si structure. According to the diffraction data, the extra atoms at octahedral sites are accommodated by a trigonal expansion of the lattice. The expansions along and normal to $[1\bar{1}1]_{Si}$ are 4·2 and 5% respectively. Since the atomic and octahedral sites of the two penetrating f.c.c. lattices together constitute a b.c.c. arrangement, the suggested η structure is trigonally distorted b.c.c., in accordance with the previous proposals for the Cu_3Si structure.

The reciprocal $(\bar{1}\bar{1}2)^*_\eta$ plane is plotted in Fig. 10(*b*) It coincides with the $(0\bar{1}0)^*_{\eta''}$ plane, which is shown in Fig. 10(*a*). The suggested fundamental reflections are enlarged. To simplify the drawings, only those matrix reflections lying outside η reflections are plotted.

4.3. *Twin formation*

In the previous section the occurrence of polycrystalline precipitates was associated with the formation of fundamental structure twins. Cu_3Si twins have previously been observed in both cast and annealed alloys, and it has been suggested that they are annealing twins generated from the transformation of η, especially from the $\eta \rightarrow \eta'$ transformation (Mima & Hasegawa, 1960). According to this assumption the

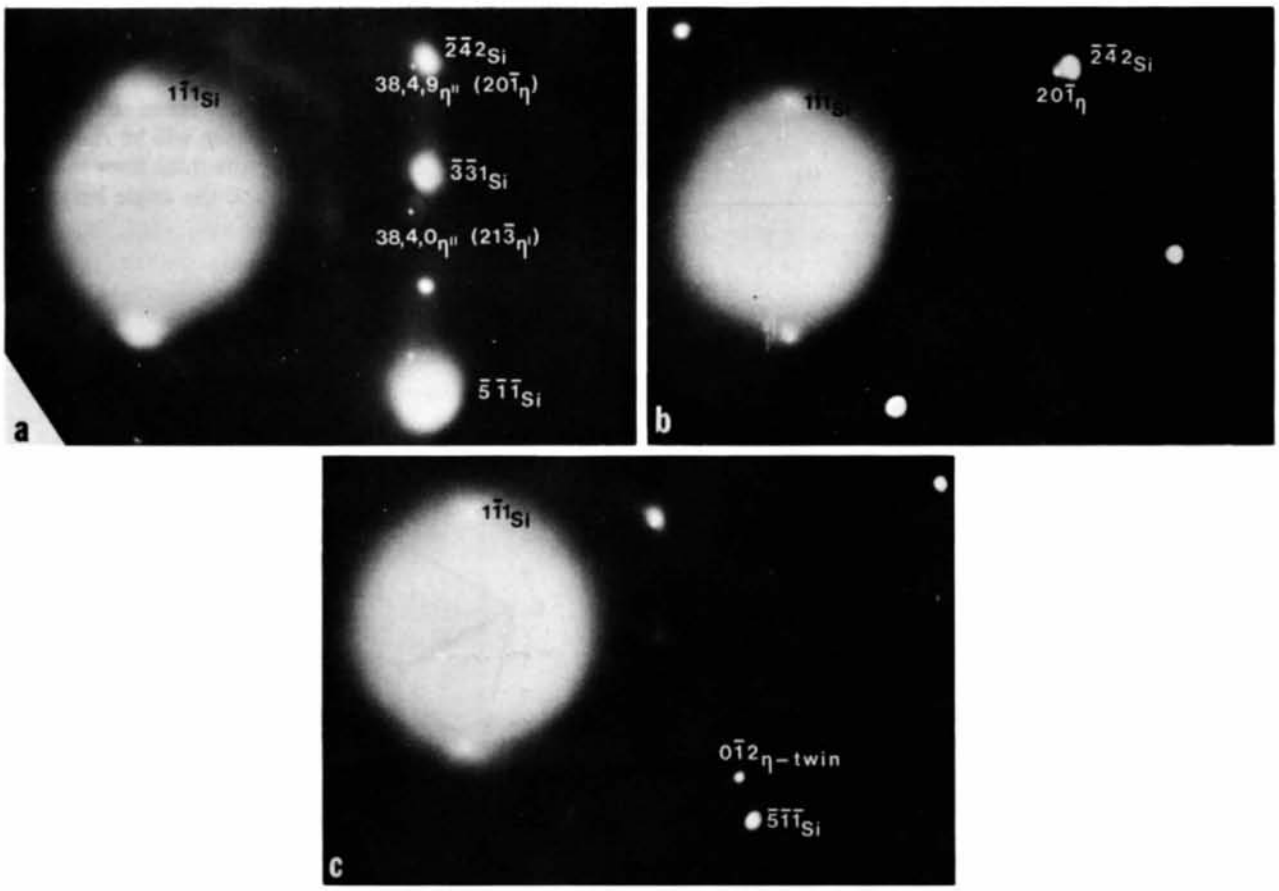

Fig. 9. Diffraction patterns indicating two orientations of the fundamental structure with respect to the matrix: (*a*) gives the true intensity of $38,4,0_{\eta''}$, (*b*) and (*c*) give the intensity of spots suggested to arise from two twin orientations of the fundamental lattice. The latter spots are seen to be much stronger than $38,4,0_{\eta''}$. All three spots originate from the same precipitate.

occurrence of polycrystalline precipitates at room temperature may stem from twin formation during the transition $\eta \rightarrow \eta'$ during cooling.

Fig. 11 shows our suggestion for the η' structure (§ 4.4) but disregarding the ordering it serves as a model for η. The strong precipitate spot in the direction of $\bar{5}\bar{1}\bar{1}_{Si}$ in Fig. 9(*c*) can be indexed according to a disordered structure in which the $(111)_\eta$ layers α and β of Fig. 11 are rotated 60° about $[11\bar{1}]_\eta$. This corresponds to a twin formation with either $(111)_\eta$ or $(11\bar{2})_\eta$ as operating twin plane. Neither of these planes is generally found as a twin plane in rhombohedral structures, but $(11\bar{2})_\eta$ corresponds to a (121) plane in the b.c.c. structure, which is considered to be the basis for Cu_3Si (see also § 4.9). B.c.c. structures nearly always have {112} planes as twin planes (Barrett & Massalski, 1966), so an association of $(11\bar{2})_\eta$ with the η twin plane seems reasonable.

The lack of visible grain boundaries inside the precipitates *A*, *B* and *C* in Fig. 4 is in accordance with a $(11\bar{2})_\eta$ twin plane, as this plane is roughly parallel to the paper in the figure. Furthermore, $(11\bar{2})_\eta$ is parallel to $\{112\}_{Si}$, and in fact, a $\{112\}_{Si}$ plane making about 10° with the incident beam intersects precipitate *D* along the well-defined 'fringe shift line' in Fig. 8.

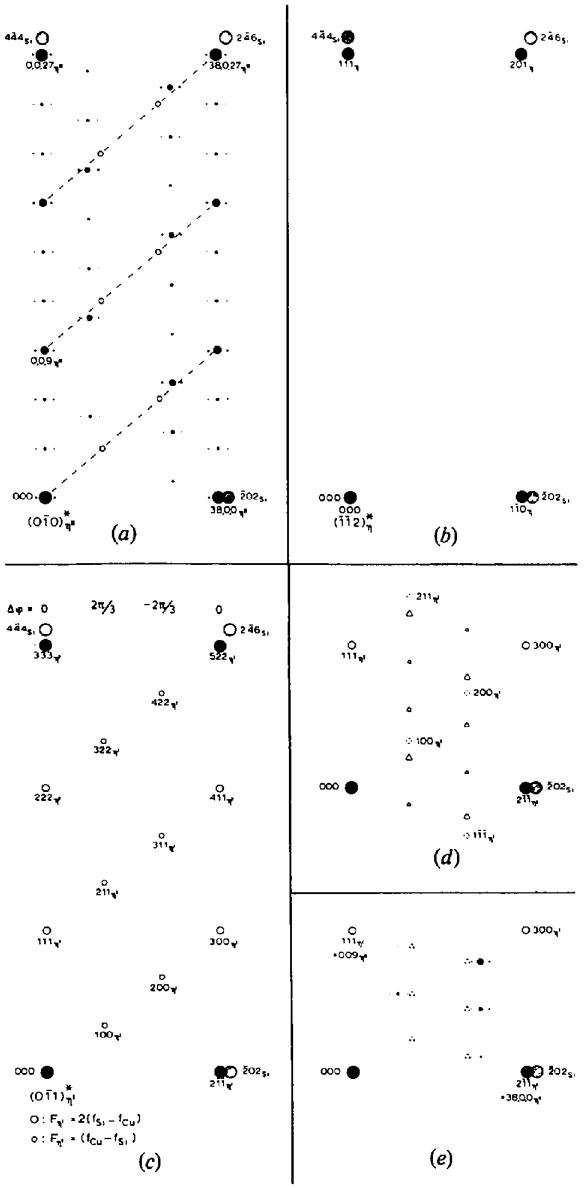

Fig. 10. The figure illustrates how the $(0\bar{1}0)^*_{\eta''}$ precipitate spot pattern in the $(121)^*_{Si}$ projection may arise through splitting of superstructure reflections: (*a*) the observed pattern, (*b*) fundamental reflections, (*c*) reflections from the superstructure, (*d*) splitting in the superstructure $[111]^*_\eta$, direction, (*e*) splitting in the superstructure $[2\bar{1}\bar{1}]^*_{\eta'}$ direction.

4.4. *The disordered η' superstructure*

Ordering and periodic displacements are assumed to lead to the additional spots between the fundamental reflections in Fig. 10(*a*). The reflections associated with the ordered η' superstructure must be located near the maxima in the intensity distribution in the reciprocal space of the η'' structure, and they should form a simple pattern. In Fig. 10(*a*), the filled and open circles which are positioned along the dashed line segments fulfil these conditions. If they are taken to be η' reflections, the structure for this phase will be rhombohedral with a unit cell as given by the thick lines in Fig. 11. The length of the unit axes and the angle between

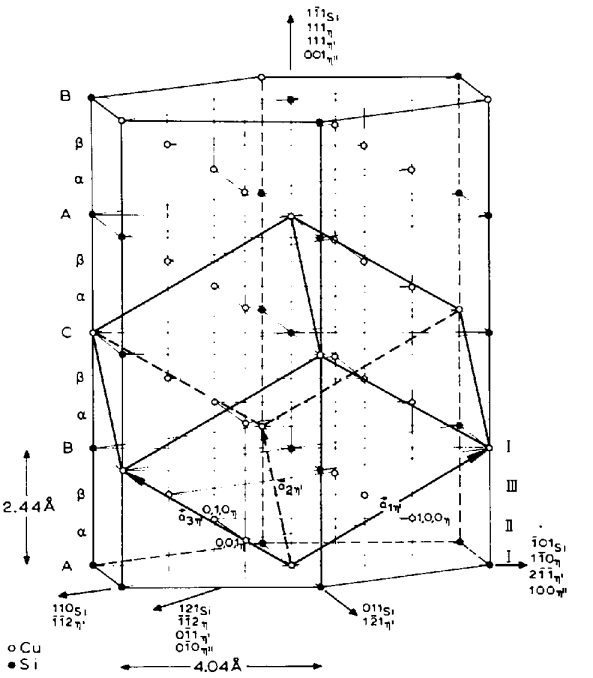

Fig. 11. The rhombohedral η' structure.

them are, respectively, $a_{\eta'} = 4{\cdot}72$ Å, $\alpha_{\eta'} = 95{\cdot}72°$, provided that there is no expansion or contraction of the lattice associated with the periodic displacements. The orientation relationships between the three Cu_3Si lattices and the Si lattice are

$$(1\bar{1}0)_{\eta}\|(2\bar{1}\bar{1})_{\eta'}\|(100)_{\eta''}\|(\bar{1}01)_{Si};$$
$$(111)_{\eta}\|(111)_{\eta'}\|(001)_{\eta''}\|(1\bar{1}1)_{Si}.$$

The space group for the suggested η' structure is $R\bar{3}$, and the ideal atomic positions, disregarding displacements due to the different nature of the atomic species, are:

Si: $2(c)\ 3$ $\frac{1}{3},\frac{1}{3},\frac{1}{3};\ \frac{\bar{1}}{3},\frac{\bar{1}}{3},\frac{\bar{1}}{3}$

Cu: $1(a)\ \bar{3}$ 0,0,0

Cu: $6(f)$ $1\ \frac{2}{9},\frac{5}{9},\frac{8}{9};\ \frac{8}{9},\frac{2}{9},\frac{5}{9};\ \frac{5}{9},\frac{8}{9},\frac{2}{9};\ \frac{\bar{2}}{9},\frac{\bar{5}}{9},\frac{\bar{8}}{9};\ \frac{\bar{8}}{9},\frac{\bar{2}}{9},\frac{\bar{5}}{9};\ \frac{\bar{5}}{9},\frac{\bar{8}}{9},\frac{\bar{2}}{9}$.

This structure has a Si content of 22 at.% (Cu_7Si_2). According to the equilibrium diagram the precipitates should, however, contain about 25 at.% Si. How this can be achieved will be discussed in § 4.7. Till then the discussion will be based on the composition 7:2.

The $(0\bar{1}1)^*_{\eta'}$ reciprocal-lattice plane – coinciding with $(\bar{1}\bar{1}2)^*_{\eta}$ – for the above atomic distribution is plotted in Fig. 10(*c*). The structure factors of the spots which are symbolized by the large and the small open circles are, respectively, equal to $2(f_{Si} - f_{Cu})$ and $(f_{Cu} - f_{Si})$; f_{Si} and f_{Cu} are the scattering amplitudes for Si and Cu atoms.

Since two twin orientations of the fundamental lattice have been present within the analyzed precipitates, there is an ambiguity in the choice of positions for the six equivalent Cu atoms in the α and β layers (§ 4.3). Referred to the η' unit axes, these positions may alternatively be

$$\tfrac{1}{9},\tfrac{4}{9},\tfrac{7}{9};\ \tfrac{7}{9},\tfrac{1}{9},\tfrac{4}{9};\ \tfrac{4}{9},\tfrac{7}{9},\tfrac{1}{9};\ \tfrac{\bar{1}}{9},\tfrac{\bar{4}}{9},\tfrac{\bar{7}}{9};\ \tfrac{\bar{7}}{9},\tfrac{\bar{1}}{9},\tfrac{\bar{4}}{9};\ \tfrac{\bar{4}}{9},\tfrac{\bar{7}}{9},\tfrac{\bar{1}}{9},$$

involving the following orientation relationship between the different lattices:

$$(0\bar{1}1)_{\eta}\|(2\bar{1}\bar{1})_{\eta''}\|(100)_{\eta''}\|(\bar{1}01)_{Si};$$
$$(111)_{\eta}\|(111)_{\eta'}\|(001)_{\eta''}\|(1\bar{1}1)_{Si}.$$

Throughout this work the analysis is based upon the first mentioned alternative for the η' structure. It will appear that the discussion of the periodic displacements is not influenced by the true orientation of the α and β layers.

4.5. *The periodic displacements normal to* $[001]_{\eta''}$

The diffraction pattern in Fig. 10(*a*) can be derived from that in Fig. 10(*c*) if periodic displacements are introduced normal to $[111]_{\eta'}$ and normal to $[2\bar{1}\bar{1}]_{\eta'}$ in the ordered superstructure. The present section deals with the displacements of the $(111)_{\eta'}$ planes, while the next section considers the long-period stacking order in the $[2\bar{1}\bar{1}]_{\eta'}$ direction.

As for close-packed structures, each of the hexagonally packed $(111)_{\eta'}$ planes occupies one of three sets of positions which we call I, II and III, given on the right in Fig. 11. The pure copper planes α and β occupy II and III positions. All the mixed-type planes occupy I positions. They are identical, but according to the sites taken up by the atomic species, they are distinguished as *A*, *B* and *C*. The stacking order *ABCABC*... is given on the left in Fig. 11.

Along the direction $[111]^*_{\eta'}$ in Fig. 10(*c*) the distance between η' spots is three times larger than the distance between visible precipitate spots in Fig. 10(*a*), suggesting that the corresponding period in real space is three times longer in the precipitates than in the proposed η' structure. A lengthening of the η' period can be performed by introducing periodic stacking faults among the $(111)_{\eta'}$ layers. Since the distance between these planes is only 0·81 Å, no faults involving shifts between the I, II and III positions are possible. The faults must therefore be introduced by modulating the stacking order of the planes *A*, *B* and *C*. No changes in atom positions will then result, and the α and β layers remain unaltered. They are therefore omitted in the further discussion.

By introducing a stacking fault at every third mixed-type plane, the period in the $[111]_{\eta'}$ direction is tripled. Two different stacking sequences are possible; *i.e.* *ABCCABBCA*... and *ABCBCACAB*.... The former of these is realized by the displacement vector $\mathbf{r}_1 = \frac{1}{3}[\bar{2}11]_{\eta'}$. The resulting stacking-fault structure is rhombohedral, and we specify it by the symbol $3R$ in analogy with long-period superlattices in close-packed metals (Sato, Toth & Honjo, 1967). As for such structures, the reciprocal-lattice lines in the stacking direction can be classified into three: the zeroth, first and second kinds, for which the displacements result in phase-angle shifts of zero, $2\pi/3$ and $-2\pi/3$, respectively, between the scattered waves from the successive layers [$\Delta\varphi$ in Fig. 10(*c*)]. Along the lines of the zeroth kind no splitting occurs. But along the two other types of lines the η' reflections are split into a series of spots [triangles in Fig. 10(*d–e*)] located at the same levels above the $(001)^*_{\eta''}$ plane as the triple spots from the η'' precipitate structure, Fig. 10(*e*). Periodic displacements normal to the $[2\bar{1}\bar{1}]_{\eta'}$ direction can therefore split the $3R$ reflections into the observed precipitate diffraction pattern.

The second stacking sequence mentioned above originates from the displacement vector $-\mathbf{r}_1 = \frac{1}{3}[2\bar{1}\bar{1}]_{\eta'}$. Hence, relative to the former stacking, this sequence introduces phase-angle shifts of opposite sign along the reciprocal lines in the stacking direction. The shifts of the split spots relative to the η' reflections will therefore be of the same magnitude as, but in opposite direction to, those in the earlier case. Thus, the spots will not lie at the same levels as the nearest precipitate triple spots, and this stacking sequence can therefore be excluded.

4.6. *The periodic displacements normal to* $[100]_{\eta''}$

In Fig. 12(*a*) the η' structure is seen viewed along $[01\bar{1}]_{\eta'} \| [010]_{\eta''}$. The α and β layers are omitted. The period along $[2\bar{1}\bar{1}]_{\eta'} \| [100]_{\eta''}$ consists of six identical planes, a'–f'. One period normal to the paper of plane a' is shown in Fig. 12(*b*), where the Cu atoms in the α and β layers are also drawn. Every other plane is displaced the vector $[0\frac{1}{2}0]_{\eta''}$ into the plane of the paper, indicated by encircled crosses.

Fig. 12(*c*) shows the same planes as Fig. 12(*a*), but includes the periodic displacements of the $(111)_{\eta'}$ planes. The new stacking sequence is given on the left. As a result of the displacements the a'–f' planes are altered, and they are denoted a–f. They are still identical, and plane a is shown in Fig. 12(*d*).

The unusual splitting described in Fig. 10(*e*) can be explained by a non-integer superperiod M which is smaller than that apparently observed. A non-integer M is achieved by a variation in the spacing between the stacking faults, so that M is the average number of planes between the faults. Such a structure is comparable to periodic antiphase structures with non-integer M (Fujiwara, 1957). This kind of long-range superperiod may explain the relatively sharp split spots from the precipitates. A precipitate with diameter 450 Å (precipitate *A*) contains only twelve half periods of the long-range stacking in the $[100]_{\eta''}$ direction. An extension of the split spots in this direction should, therefore, be expected. However, in the above model, the splitting is determined by the average distance between each stacking fault, which is less than the

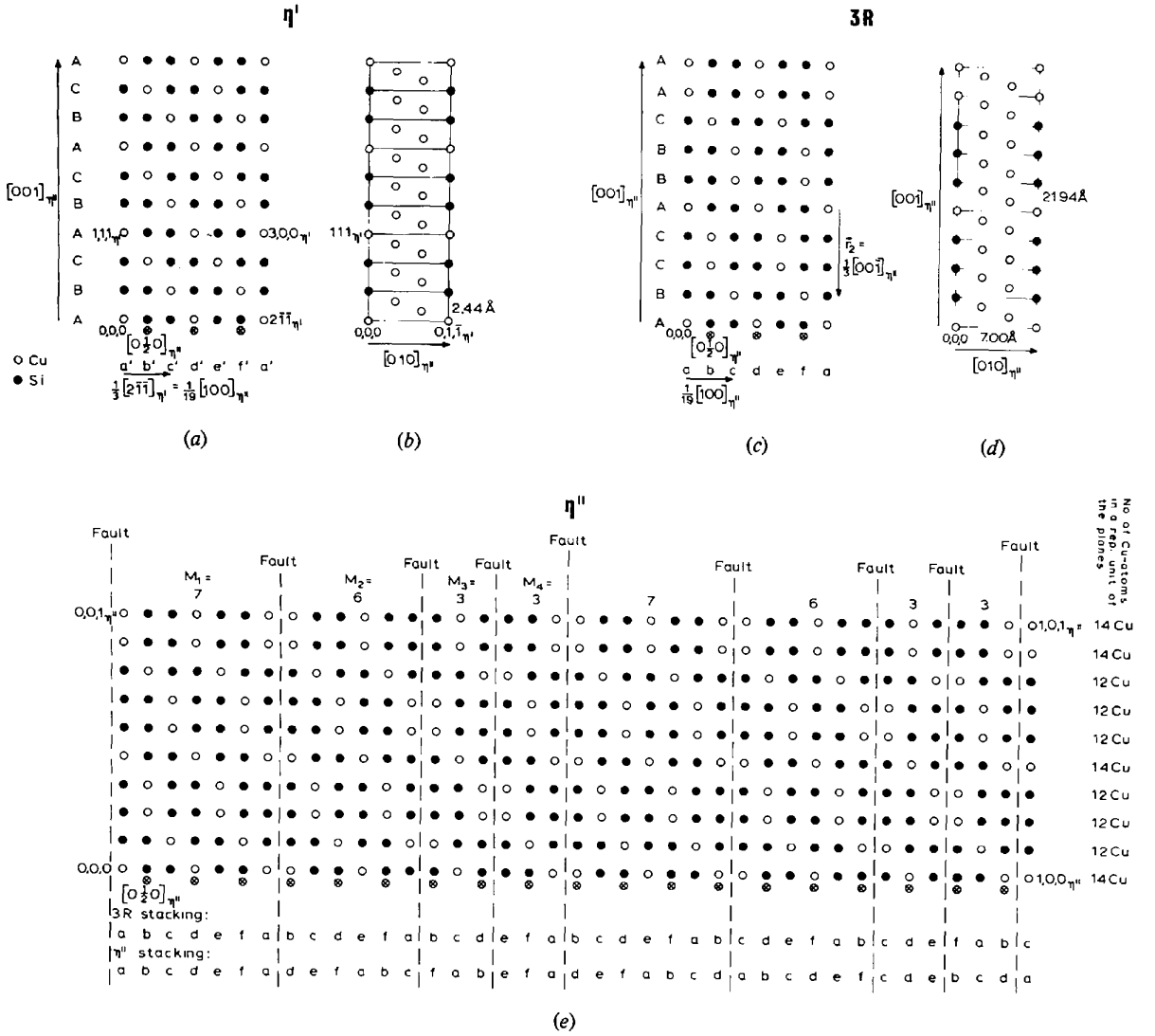

Fig. 12. The Cu_3Si structure. Viewed along $[010]_{\eta''}$: (*a*) the η' superstructure, (*c*) the 3*R* structure and (*e*) the η'' structure arising from the stacking sequence 7633... along $[100]_{\eta''}$. (*b*) and (*d*) show one period normal to the paper of the η' a' plane and the 3*R* *a* plane respectively. In (*a*), (*c*) and (*e*) the Cu atoms in the α and β layers are omitted.

superlattice half period, and sharper split reflections result.

In this case too we assume that the displacements do not alter the atomic positions. This restricts the displacement vector $\mathbf{r}_2$ to be either a vector along $[001]_{\eta''}$ or to be equal to $[0\,\frac{1}{3}\,\frac{2}{27}]_{\eta''}$ or $[0\,\frac{1}{3}\,\frac{\bar{1}}{27}]_{\eta''}$. From intensity calculations the structure models deduced from the two last vectors could readily be excluded. Numerous stacking sequences can be formed with $\mathbf{r}_2$ parallel or antiparallel to $[001]_{\eta''}$. Let $M_1, M_2, \ldots, M_n$ ($M_1 + \cdots + M_n = 19$) be the number of planes between successive faults in the halfperiod. Generally, several values of $\mathbf{r}_2$ are possible for each choice of n. As an example, one of the possible sequences for $n = 4$, *i.e.* $M = 4{\cdot}75$, is shown in Fig. 12(*e*). For this n the only possible displacement vector is $\mathbf{r}_2 = [00\frac{\bar{1}}{3}]_{\eta''}$. In Fig. 12(*e*) $M_1, \ldots, M_n$ are chosen equal to 7, 6, 3, 3, and the stacking faults are marked by the dashed lines. The original and the new stacking sequences are given below the planes.

A series of stacking sequences were produced by varying n and $M_1, \ldots, M_n$ systematically. Although a number of n values ($n = 3, 4, 6, 7$) gave intensity distributions comparable to the experimental one, best agreement with the experimental results was obtained for $n = 4$. Several M_1–M_4 combinations gave satisfactory results, including $M_1 \ldots M_4 = 8553$; 8443; 8434; 7633; 7534; 7552; 7543 and the corresponding sequences with the M_j's in reversed order. As an example, the calculated intensity distributions along the lines $10,0,l_{\eta''}$, $28,0,l_{\eta''}$ and $h07_{\eta''}$ for the sequence 7633 are given in Fig. 13(*a,b,c*). The three last M_j values in this sequence correspond to a whole and a half period in the η' and $3R$ lattices along the stacking direction, and may therefore be the sequence which is found in the precipitates. The calculated intensities are seen to fit the experimental values quite well. The experimental intensities along $28,0,l_{\eta''}$ follow roughly the periodic variation depicted in Fig. 13(*b*). The anomalous intensity distribution observed along $10,0,l_{\eta''}$ is similar to the theoretical one, and is due to the fact that $(f_{Cu} - f_{Si})^2$ takes the minimum value zero for reciprocal vectors practically equal in length to $|[10,0,2]_{\eta''}|$, f_{Cu} and f_{Si} being atomic scattering amplitudes for electrons. For the same reason a low intensity was observed for the smallest $|l|$ values along $91l_{\eta''}$, and a similar depression of the reflection $\bar{1}0,0,7_{\eta''}$ is seen in Fig. 13(*c*). The exceedingly weak spots in Figs. 13(*a*)–(*b*) (*e.g.* $28,0,11_{\eta''}$) arise from a periodic varying composition of the $(001)_{\eta''}$ planes, introduced by the stacking faults along $[100]_{\eta''}$, Fig. 12(*e*) to the right.

In Fig. 13(*c*) the triangles denote the positions of the $3R$ superlattice reflections in Fig. 10(*d*)–(*e*). Each $3R$ reflection splits into every fourth spot along the row, including respectively $\bar{1}0,0,7_{\eta''}$ and $28,0,7_{\eta''}$. The enveloping curves for each set of split spots are drawn, and it is seen that an intensity increase close to the $3R$ reflections results in the observed weak split spots. A relatively high intensity is also calculated for some reflections outside the triplets plotted in Fig. 3, *e.g.* for $22,0,7_{\eta''}$ and $32,0,7_{\eta''}$. This is not in contradiction to the experimental results because the existence of the weak split spots was experimentally established mainly from interference contrast in dark-field micrographs. Most of the weak split reflections are probably invisible in the diffraction patterns. The observed intensity in them is apparently mainly due to multiple scattering.

The other sequences which were mentioned above possess very similar intensity distributions in reciprocal space. Owing to the limited experimental results the correct stacking sequence cannot be picked out on the basis of the calculations. Nevertheless, 7633 is tentatively suggested to be the most probable one since it contains one whole and two half periods of the $3R$ structure.

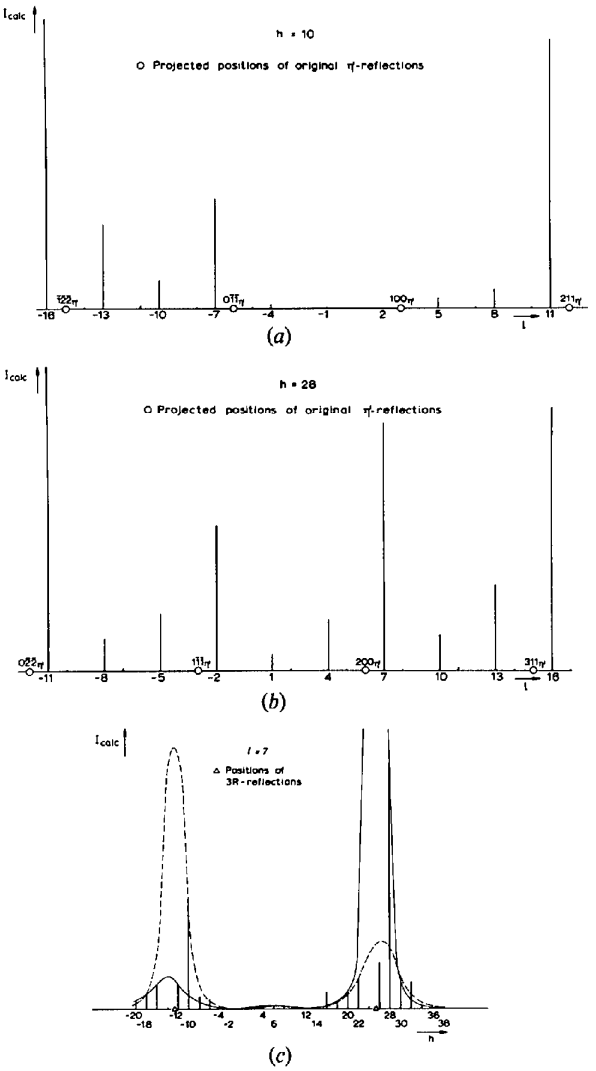

Fig. 13. Calculated relative intensities along (*a*) $10,0,l_{\eta''}$, (*b*) $28,0,l_{\eta''}$ and (*c*) $h07_{\eta''}$ for the structure given in Fig. 12(*e*).

4.7. *Vacancies/atomic composition*

The average volume per atomic position in the proposed precipitate structure is 11·5 Å^3. For the known Cu–Si structures the atomic volume increases slowly from 11·6 to 12·0 Å^3 when the Si concentration increases from about 13 to 20 at.%. This predicts a corresponding value of 12 Å^3, or slightly higher, for η-Cu_3Si. The small value, 11·5 Å^3, indicates that a large number of vacancies are dissolved in the structure. An estimate of the minimum concentration of vacancies in the precipitate phase can be made, assuming that the relaxations around the empty sites are so large that all the atoms are evenly spaced, *i.e.* that no vacancies can be 'seen' in the structure. If the volume of one atom is 12 Å^3, a fraction, 11·5/12, of the atomic positions will be occupied by atoms under these conditions, giving a vacancy concentration of about 4%. This is the lower limit for the vacancy content since vacant sites are likely to occupy some volume of the crystal.

In the previous sections a lattice containing 22 at.% Si has been described, while the equilibrium diagram predicts 25 at.% Si. On the basis of the preceding paragraph one might suggest that the 25 at.% Si has been achieved by leaving one of seven copper positions vacant (11% vacancies). Intensity calculations show, however, that a random distribution of vacancies at Cu positions destroys the observed $(f_{Cu} - f_{Si})^2$ proportionality in the superstructure reflections. An ordering of 11% vacancies on Cu sites is expected to have a similar effect in reciprocal space. In fact, the accurate $(f_{Cu} - f_{Si})^2$ proportionality observed along the reciprocal lines $10,0,l_{\eta''}$ and $91l_{\eta''}$ is a strong indication of a completely disordered distribution of vacancies.

It is suggested that the high silicon content is achieved by a disordered distribution of silicon at the Cu positions. Three alternative distributions exist. The additional silicon may be randomly distributed (i) at all the Cu sites, (ii) among the six equivalent Cu sites in the α and β layers or (iii) at the Cu origin positions $[1(a)\,\bar{3}]$ of the η' cells. By comparing calculated and observed intensities the third possibility has been excluded (Solberg, 1975, pp. 125–126). The first two alternatives cannot be distinguished on the basis of the experimental results. However, since the Cu sites in the mixed-type atom planes are very different from those in the α and β layers, the second possibility is considered to be the true distribution.

It is worth noticing that a distribution of silicon at the Cu sites seems to fit in with the phase diagram (Mima & Hasegawa, 1960; Elliot, 1965). With decreasing temperature a sudden decrease in the Si content occurs for each phase transformation. Since the degree of order increases with decreasing temperature, an ejection of additional and randomly distributed silicon should be expected for each phase transformation.

4.8. *Atomic displacements*

In the previous sections, atomic displacements from the average positions are not considered. Such displacements will be present in the η' structure because of the different natures of the atomic species. Furthermore, the stacking faults change the symmetry of the crystal, resulting in additional atomic displacements. The observed $00l_{\eta''}$ satellites are probably caused by such displacements. Similarly, satellites corresponding to $200_{\eta''}$ and $209_{\eta''}$ may arise from lattice modulations caused by the long-period stacking in the $[100]_{\eta''}$ direction (*cf.* Okamura, Iwasaki & Ogawa, 1968).

It is not expected that the relatively simple model for the η'' structure given in the previous sections can account for all details in the intensity distribution in reciprocal space. However, the $00l_{\eta''}$ satellites suggest that the changes accompanying the periodic displacements are quite large. Together with the atomic displacements which are already present in the basic η' structure such changes can probably account for the existing discrepancies between the observed and the calculated intensities, *e.g.* the high observed intensity in $28,0,\bar{5}_{\eta''}$.

4.9. *The origin of the long periods*

Long-period superstructures are usually electron phases which obtain their stabilization by a reduction in the energy of the free electrons through a splitting of Brillouin zone boundaries (Sato & Toth, 1961). Since the Cu–Si compounds are regarded as electron phases, and since the phase diagram suggests that the periodic stacking faults represent an equilibrium state, the same mechanism is supposed to be the origin of the long-period stacking modulations in η''-Cu_3Si. Many features of the proposed Cu_3Si structure indicate that it is an electron compound of the δ type. Like electron δ phases (Hume-Rothery & Raynor, 1954) it has a structure which is based on the body-centered cube, a modification of the general γ type of structure. Distorted non-cubic modifications of the γ structure are also found in other systems, *e.g.* δ-Cu_9In_4 (Reynolds, Wiesman & Hume-Rothery, 1951–52; Hellner & Laves, 1947; Corderoy & Honeycombe, 1963–64). Like Cu_3Si, Cu_9In_4 contains possibly some modulation of a superlattice (Corderoy & Honeycombe, 1963–64). Furthermore, the homogeneity range of δ phases lies generally above the e/a limit (1·70) commonly associated with γ phases, and consequently they are usually characterized by the presence of ordered or, usually, randomly distributed lattice vacancies (Hume-Rothery & Raynor, 1954; Massalski & King, 1961). For Cu_3Si the electron/atom ratio is equal to 1·75, and it probably contains a large number of vacancies. A vacancy concentration of about 7% at the phase

boundary towards silicon will reduce the number of valence electrons in a volume corresponding to the γ-brass unit cell (54 atom sites) to 88, which appears to be the critical limit for normal γ structures (Hume-Rothery & Raynor, 1954). Since the minimum vacancy content in § 4.7 was found to be about 4%, a value of 7% seems plausible. The vacancy concentration is expected to decrease with decreasing silicon content.

Further evidence that stacking modulations may occur in deformed γ-brass structures is provided by the low-temperature η-Cu–Sn, which has an orthorhombic structure that can be regarded as a superlattice on a NiAs-type structure (Schubert, Kiefer, Wilkens & Haufler, 1955; Bernal, 1928; Westgren & Phragmén, 1928; Carlsson & Hägg, 1932). There is a close relationship between the γ-brass and the NiAs structures (the regions in the Periodic Table in which the two are formed overlap).

From its structural characteristics the Cu_3Si phase should have been denoted δ, and not η as is common. In the Cu–Si system the intermediate phases appear to have been erroneously named, according to the nomenclature which is adopted for the electron phases. Only the β phase is given the same name as the corresponding compound in the typical electron phase systems. A modification of the names of the Cu–Si intermediate phases to the common electron-phase nomenclature would be appropriate (Solberg, 1975, pp. 131–135).

According to the theory for electron phases, a variation in length of the two superperiods in η''-Cu_3Si is expected to occur with composition, so the precipitate structure is probably one out of many variants of the η''-phase. The precipitates are located at the phase boundary towards the Si-rich side of the equilibrium diagram. Hence, the periods determined in §§ 4.5 and 4.6 should be considered as extremal values.

5. Conclusion

By electron diffraction and microscopy it has been shown that copper precipitates in silicon are of the equilibrium Cu_3Si phase. Consistent with the available X-ray diffraction data for this phase, the crystal structure of the precipitates is determined to be based on a trigonally deformed body-centered cubic arrangement. It probably contains a larger number of vacancies, and is consequently characterized by the features which are typical for electron δ phases. At room temperature the precipitates have a two-dimensional long-period superlattice, and are suggested to be of the low-temperature Cu_3Si polymorph (η''). It is proposed that the high-temperature η phase is disordered, and that the intermediate-temperature η' phase has an ordered superstructure. The precipitate lattice is assumed to originate from periodic displacements in the η'-phase. On the basis of the diffraction data for the precipitates the following unit-cell parameters for the three polymorphs are suggested:

η: trigonal, space group $R\bar{3}m$, $a_\eta = 2{\cdot}47$ Å, $\alpha_\eta = 109{\cdot}74°$.

η': trigonal, space group $R\bar{3}$, $a_{\eta'} = 4{\cdot}72$ Å, $\alpha_{\eta'} = 95{\cdot}72°$.

η'': orthorhombic (C), $a_{\eta''} = 76{\cdot}76$, $b_{\eta''} = 7{\cdot}00$, $c_{\eta''} = 21{\cdot}94$ Å.

The superperiods in the η'' phase are expected to vary with the composition, so the precipitate structure is probably just one out of a large number of variants of the η''-Cu–Si structure. The atomic distributions in the η and η' phases as well as the periodic displacements present in the precipitates have been discussed.

The author is very much indebted to Dr J. Gjønnes, Dr E. Nes and cand.real. Arne Olsen for stimulating discussions.

References

ARRHENIUS, S. & WESTGREN, A. (1931). *Z. Phys. Chem. Abt. B*, **14**, 66–79.

BARRETT, C. S. & MASSALSKI, T. B. (1966). *Structure of Metals*, p. 414. New York: McGraw-Hill.

BERNAL, J. D. (1928). *Nature (London)*, **122**, 54.

CARLSSON, O. & HÄGG, G. (1932). *Z. Kristallogr.* **83**, 308–317.

CORDEROY, D. J. H. & HONEYCOMBE, R. W. K. (1963–64). *J. Inst. Met.* **92**, 65–69.

DAS, G. (1973). *J. Appl. Phys.* **44**, 4459–4467.

ELLIOT, R. P. (1965). *Constitution of Binary Alloys, First Supplement*, p. 385. New York: McGraw-Hill.

FIERMANS, L. & VENNIK, J. (1965). *Phys. Status Solidi*, **12**, 277–289.

FIERMANS, L. & VENNIK, J. (1967*a*). *Phys. Status Solidi*, **21**, 627–634.

FIERMANS, L. & VENNIK, J. (1967*b*). *Phys. Status Solidi*, **22**, 463–471.

FUJIWARA, K. (1957). *J. Phys. Soc. Jpn*, **12**, 7–13.

GJØNNES, J. & SOLBERG, J. K. (1978). *J. Appl. Cryst.* **11**, 190–192.

HANSEN, M. (1958). *Constitution of Binary Alloys*. Metallurgy and Metallurgical Engineering Series, pp. 629–633. New York: McGraw-Hill.

HELLNER, E. & LAVES, F. (1947). *Z. Naturforsch. Teil A*, **2**, 177–183.

HUME-ROTHERY, W. & RAYNOR, G. W. (1954). *The Structure of Metals and Alloys*, pp. 202–210. London: The Institute of Metals.

MASSALSKI, T. B. & KING, H. W. (1961). *Prog. Mater. Sci.* **10**, 1–78.

MIMA, G. & HASEGAWA, M. (1956). *Technol. Rep. Osaka Univ.* **6**, 313–321.

MIMA, G. & HASEGAWA, M. (1957). *Technol. Rep. Osaka Univ.* **7**, 385–397.

MIMA, G. & HASEGAWA, M. (1960). *Technol. Rep. Osaka Univ.* **10**, 157–169.

NES, E. (1974). *Acta Metall.* **22**, 81–87.

NES, E. & SOLBERG, J. K. (1973*a*). *J. Appl. Phys.* **44**, 486–487.

NES, E. & SOLBERG, J. K. (1973*b*). *J. Appl. Phys.* **44**, 488–489.

NES, E. & WASHBURN, J. (1971). *J. Appl. Phys.* **42**, 3562–3574.

NES, E. & WASHBURN, J. (1972). *J. Appl. Phys.* **43**, 2005–2006.

NES, E. & WASHBURN, J. (1973). *J. Appl. Phys.* **44**, 3682–3688.

OKAMURA, K., IWASAKI, H. & OGAWA, S. (1968). *J. Phys. Soc. Jpn*, **24**, 569–579.

REYNOLDS, J., WIESMAN, W. A. & HUME-ROTHERY, W. (1951–52). *J. Inst. Met.* **80**, 637–640.

RIEGER, H. (1964). *Phys. Status Solidi*, **7**, 685–699.

SATO, H. & TOTH, R. S. (1961). *Phys. Rev.* **124**, 1833–1847.

SATO, H., TOTH, R. S. & HONJO, G. (1967). *J. Phys. Chem. Solids*, **28**, 137–160.

SCHUBERT, K. & BRANDAUER, G. (1952). *Z. Metallkd.* **43**, 262–268.

SCHUBERT, K., KIEFER, B., WILKENS, M. & HAUFLER, R. (1955). *Z. Metallkd.* **46**, 692–715.

SOLBERG, J. K. (1975). *Precipitation of Interstitially Dissolved Copper in Dislocation-Free Silicon.* Thesis, Univ. Oslo.

SOLBERG, J. K. & NES, E. (1978*a*). *Philos. Mag.* In the press.

SOLBERG, J. K. & NES, E. (1978*b*). *J. Mater. Sci.* In the press.

WESTGREN, A. & PHRAGMÉN, G. (1928). *Z. Anorg. Chem.* **175**, 80–89.

Acta Cryst. (1978) A**34**, 698–701

Destruction of Pseudo-Centrosymmetry with Direct Methods

BY ROLF KARLSSON

Department of Structural Chemistry, Arrhenius Laboratory, University of Stockholm, S-106 91 Stockholm, Sweden

(*Received* 27 *April* 1977; *accepted* 15 *March* 1978)

Phase refinement based on minimization of $C = \Sigma_{\mathbf{h},\mathbf{k}}|E_{\mathbf{h}}E_{\mathbf{k}}E_{-\mathbf{h}-\mathbf{k}}|[1 - \cos(\varphi_{\mathbf{h}} + \varphi_{\mathbf{k}} + \varphi_{-\mathbf{h}-\mathbf{k}})]^2$ has been tested on several known structures (space group $P2_1$) containing elements of pseudo-centrosymmetry. C always has a maximum for a consistent centric phase set provided that some invariants have a phase of 180°. Thus C will have a minimum for a noncentric phase set, and the phases do not turn centric during the refinement as often is the case when the ordinary tangent formula is applied. The hydrochloride of the insect alkaloid adaline (space group $P2_1$), whose cell constants and hitherto unpublished atomic positions are given, is one of the examples upon which the destruction of centrosymmetry is demonstrated. The destruction of centrosymmetry was indicated by the largest maximum of a one-dimensional modified F^2 synthesis along the unique axis.

Introduction

A non-centrosymmetric structure containing a centrosymmetric arrangement of atoms in the unit cell, such as one or two Br atoms among several C and O atoms, represents a problem of pseudo-centrosymmetry. It is a common experience that the tangent formula has difficulties in refining phases of such structures, especially if there are no reflexions with phase restrictions, and it often ends up with centric phases even if the refinement starts with known phases. Normally the centrosymmetry is broken by the extraction of a part of the structure from the Fourier map based for instance on centric heavy-atom phases. The full structure is then obtained by successive Fourier synthesis. This process is automatically carried out in the phase-correction method (Hoppe & Gassman, 1968). Karle & Karle (1969) showed how the difficulties with the tangent formula were met in the structure solution of an alkaloid $C_{31}H_{38}NO_6Br$, in space group $P2_12_12_1$ with Br at x,0,0. Keeping phases computed from the bromobenzoate group fixed, phases for additional reflexions were obtained by the tangent formula. The E map computed from these phases was claimed to be better resolved than that based on bromobenzoate phases alone. Busetta (1976) tested a modification of the tangent formula to meet this problem with alborixin, $C_{48}H_{84}O_{14}K$ (space group $P2_1$; $Z = 2$) for which two thirds of the 406 phases with $|E| > 1{\cdot}60$ differed by less than 30° from the most similar centric solution. This article will describe an alternative method to solve such problems.